Relevence of 3D simulations and sandwich core topology for the modeling of honeycomb core sandwich panels undergoing mode I delamination

Daniel Höwer[a,*], Kumar C. Jois[a], Bradley A. Lerch[b], Brett A. Bednarcyk[b], Evan J. Pineda[b], Stefanie Reese[a], Jaan-Willem Simon[a]

[a] *Institute of Applied Mechanics, RWTH Aachen University, 52074 Aachen, Germany*
[b] *NASA Glenn Research Center, Cleveland, OH 44135, USA*

Abstract

A recently developed cohesive zone traction-separation law, which includes the effects of fiber bridging in a novel way, is extended from 2D to 3D. The proposed cohesive model is applied to low fidelity (i.e. homogenized core representation) and high fidelity (i.e. directly accounting for the core topology) finite element models of a composite panel comprised of carbon fiber reinforced plastic facesheets and a honeycomb sandwich core. This enables the investigation of 2D to 3D parameter transferability, width-dependent effects such as thumbnail-shaped crack growth, and the verification of plane strain / plane stress assumptions. A pronounced curvature of the initial interface-related crack front is observed, while the bridging-related crack front is straight. Furthermore, it is found that the cohesive parameters can easily be transferred from 2D to 3D under plane stress assumptions, but not under plane strain assumptions. The numerical predictions are compared to experimental load-displacement and R-curves.

Keywords: delamination, single cantilever beam, cohesive zone modeling, fiber bridging

*Email: daniel.hoewer@rwth-aachen.de

1. Introduction

The payload of launch vehicles is protected from aerodynamic and acoustic loads during launch through payload fairings, i.e. large shell structures which are mounted atop the structure. The baseline design of the payload fairing for NASA's Space Launch Systems (SLS) heavy lift vehicle involves separable petals composed of aluminum honeycomb sandwich panels with carbon fiber reinforced polymer facesheets. There are a number of requirements and challenges which need to be adressed in order to ensure that the expected life and performance of honeycomb structures like the SLS fairing is not jeopardized. For instance pre-existing flaws from manufacturing defects or damage during handling, assembly, payload encapsulation, vehicle integration and launch can impair the ability of the fairing to fulfil its purpose: Protecting the payload during launch and ensure a clean fairing separation from the vehicle after launch, without the possibility of re-contact. A number of pre-existing defects can be detected through non-destructive evaluation prior to launch will be repaired. However, the presence of undetected damage, as well as damage occurring during launch, cannot be ruled out. Therefore, damage tolerance is a key component of the SLS fairing design.

Among the most prevalent causes of post-manufacturing damage are low-speed impacts, such as tool drops or unintended contact with ground support equipment. In the case of honeycomb sandwich structures, low-speed impacts result in core crushing, delamination/disbonds, and matrix cracking [1, 2]. This can be the cause of kink band formation (fiber microbuckling), indentation (core crushing growth), and delamination/disbond growth [1–4] during subsequent loading. The effect of such damage on composite honeycomb sandwich panels is typcically quantified through compression after impact (CAI) tests. CAI tests produce a reduced design-to strength allowable for the honeycomb panel composite facesheets, providing damage tolerance for strength-driven designs [5, 6]. However, the acreage payload fairing panel design is buckling-dominated, with local stresses at the buckling failure loads being several times lower than the

strength allowable [7–9]. As such, understanding the failure mechanisms associated with damage and buckling is critical for providing damage tolerance to large composite honeycomb sandwich structures like the SLS fairing. This point is further emphasized by observations that, for a large number of lightweight designs, delamination is one of the most critical modes of failure [10, 11] as it limits the performance of composites in safety-critical structures e.g. due to the buckling of delaminated sandwich beams [12, 13].

The established methods to characterize the mode I delamination resistance of laminates are the double cantilever beam (DCB) and single cantilever beam (SCB) tests according to ASTM D 5528 [14]. The standard requires the determination of the current crack length by means of a moving telescope or similar devices. One of the implications of this fact is that the measurements will be inaccurate when the crack front is not straight. It has been shown [15–18] that the crack front should be curved due to anticlastic bending, and the curvature of the delamination crack front of DCB specimens has been subject to extensive research. In the pioneering papers on the curvature of the delamination front, Davidson and Schapery [16–18] derived shapes of the crack front curvature dependendent upon the facesheet layup and compared the results to finite element (FE) calculations. The shape of the crack front was shown to be predominantly driven by the degree of anisotropy of the levers, since this is the main determinant of anticlastic bending. The anticlastic bending leads to a saddle-shaped deformation of the levers and the crack front therefore propagates further at the centerline of the specimen compared to the edges of the specimen. This concept has been used and recently extended by e.g. Shokrieh et al. [15] where the focus was finding correction factors which permit a calibration of experimental data to the true values. Very recently, Reiner et al. [19] used digital image correlation (DIC) to conduct a top surface analysis of a DCB in order to obtain in situ measurements of the delamination front of DCB specimen during ASTM D5528 tests. Krull et al. [20] used a light source and overhead and side-mounted cameras to determine the crack curvature of translucent continuous glass fiber-reinforced DCB specimen and Adams et al. [21] used dye penetrant

to mark the crack progression and crack curvature of foam core SCB specimen. However, the latter method is feasible neither for continuous crack monitoring nor for honeycomb core specimens. In summary, the curvature of the delamination front of DCB and SCB specimen is well-documented, but still subject to research.

While monolithic laminates have received a great deal of attention, the delamination of sandwich panels in general and, in particular, the delamination front curvature, has received much less attention and the definition of a test standard is still an active research topic [21]. Ratcliffe and Reeder [22] proposed a single cantilever sizing method based on an analytical representation of the SCB on an elastic foundation. From this solution they derived a list of 11 limitations for e.g. the intact specimen length, specimen width, minimum thickness of the facesheet, which can be used as a guideline for the sizing of an SCB specimen. This work is continued by Rinker et al. [23] where an extensive experimental investigation the effect of the honeycomb cell size, facesheet thickness and specimen width of SCB carbon fiber reinforced plastic (CFRP) facesheet honeycomb core sandwich panels was conducted. Rinker et al. [23] further raised several important questions for future research. Of these, the two most important questions with respect to the current investigation are: 1.) Are the plane strain boundary conditions, which are assumed in the data reduction, met in the experiment? 2.) Is it valid to smear the meso-level strain and stress distribution of the highly inhomogeneous honeycomb structure over the cross-section? In addition, the authors numerically investigated the effect of initial disbond radii and facesheet thickness on the mode I ground-air-pressurization-driven facesheet/core delamination of honeycomb sandwich panels in [24].

A number of authors have published research on the experimental determination of the cohesive parameters of honeycomb core sandwich panels. Ural et al. [25] for instance, use flatwise tension tests in order to determine the cohesive strength of the honeycomb core to composite facesheet interface and DCB tests in order to characterize the fracture toughness. They find a remarkable difference in fracture toughness values between bag side and tool side. Shivakumar

et al. [26] compare various testing conditions, like the cracked sandwich beam test, the SCB and tilted sandwich debond test as well as multiple data reduction techniques like modified beam theory (MBT), compliance calibration method (CC) and modified compliance calibration method (MCC) [27]. Both MBT and MCC were found to give virtually identical results and Shivakumar and Smith [26] therefore recommend the usage of MBT due to its simplicity, as done in the present paper. It is of note that, some authors mention the propagation of the crack into the core from the interface [21] or even from the interface into the interface between the plies of the facesheet [28] and find a number of influence parameters.

Numerically, delamination is typcically modeled by using zero-thickness cohesive zone models (CZM) which relate the separation of two surfaces to a traction that acts between the surfaces. The traction-separation law can have a bilinear [29, 30], tri-linear [31–36], quadratic [37], square root [38], exponential [39, 40] or power law shape [41, 42]. Alternatively, finite thickness delamination at moderate failure strains can be treated in a suited continuum damage framework [43–46] or through a strategy which combines cohesive zone modeling and extended finite elements [47]. A comprehensive overview of methods to incorporate failure in a composite context is provided by Orifici et al. [48] and in terms of more general traction-separation relationships across fracture surfaces by Park and Paulino [49] as well as Dimitri et al. [50].

When fiber bridging is to be accounted for in the CZM framework, this is usually accomplished by a tri-linear traction-separation relationship. Noteworthy examples of this technique have been published by, for instance, Li et al. [31–33] and Dávila et al. [34]. These approaches have proven very reliable for solid laminates. However, it has recently been shown by Höwer et al. [51, 52] that the delamination between CFRP facesheet and honeycomb core can be captured more accurately in terms of the load-displacement curve and local strain distribution by a two component cohesive law in which a conventional cohesive law (e.g. exponential softening) represents the initial debonding and a newly developed bridging component captures the cohesive behavior at higher sepa-

rations. This modeling approach proved to have a number of advantages: it reduced the relative error in the region between the onset of damage - i.e. the first non-linearity of the global load-displacement curve - and the peak load by up to 50 percentage points compared to the best fit with some standard cohesive formulations. Furthermore, the newly proposed formulation was highly computationally efficient, as shown by a wall-clock time reduction of more than 50% compared to the Abaqus COH3D8 elements, and local strain patterns seen in experiments were captured much more accurately.

As a 2D model was previously used, the influence of 3D effects as well as the effects of the topology of the honeycomb core were not included so far. Furthermore, the suitability of plane stress or plane strain assumptions for the SCB specimen needs to be clarified and the parameter transferability from 2D to 3D (high and low fidelity) has to be shown, which is another aim of this paper. Höwer et al. used the plane stress assumption to model the SCB sandwich panel in previous work [51]. However, in the literature the DCB specimen for instance is modeled using plane strain [53, 54] as well as plane stress assumptions [55, 56], which suggests that the issue must be addressed for the SCB as well.

2. Single Cantilever Beam (SCB) specimen

2.1. Experimental setup

As previously described in [51], a 609.6 mm by 609.6 mm honeycomb sandwich panel was manufactured from IM7/8552-1 prepreg tape and 49.66 kg/m^3 Hexcel 5052 aluminum honeycomb core with a 0.0178 mm foil gauge, 3.175 mm cell size, and a 25.4 mm height. The facesheets were comprised of eight plies each, which were hand-laid with a $[45°/90°/-45°/0°]_s$ stacking sequence. The facesheet/core adhesion was achieved through FM-300K film adhesive between the constituents. To form the initial disbond between the core and the upper facesheet, a 101.6 mm wide Teflon strip was placed between the facesheet and the film adhesive at the middle of the panel along the entire 609.6 mm length in one direction. The panel was subsequently bagged and co-cured in an autoclave

following a standard pressure/temperature profile.

The SCB testing was performed on a load frame under quasi-static displacement control at a rate of 0.42 mm/s up to 44.48 N and after this at a decreased rate of 0.021 mm/s. Samples were subjected to a single precracking load/unload cycle to ensure a sharp crack tip for the subsequent loading.

Crack length identification and data reduction was done in accordance with ASTM D 5528 [14]. A schematic of the setup is provided in Figure 1 and an actually tested specimen is shown in Figure 2.

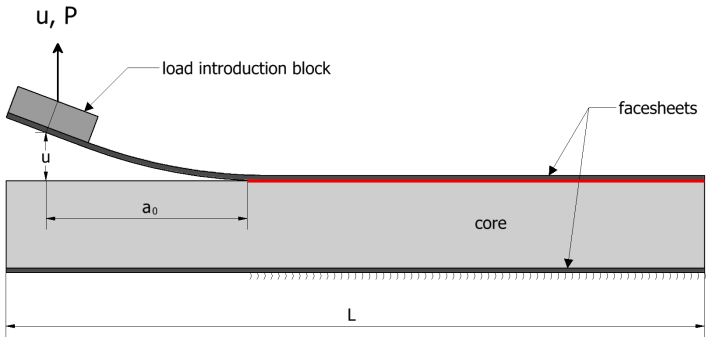

Figure 1: Schematic of the 2D finite element model. The cohesive layer is shown in red. Except for the thickness of the cohesive layer the drawing is true to scale.

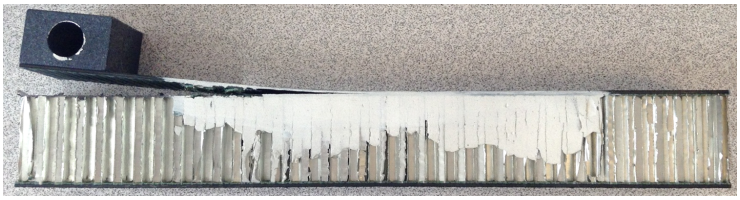

Figure 2: Photograph of a SCB specimen after testing.

2.2. SCB finite element model representations

Primarily, four distinct finite element models are considered: (i) The 2D model (Figures 1 and 3) subjected to plane stress boundary conditions; (ii) The

2D model (Figure 1 and 3) subjected to plane strain boundary conditions; (iii) the 3D low fidelity (LoF) model (Figure 4); (iv) the 3D high fidelity (HiF) model (Figure 5). Further variations of these four baseline models were investigated

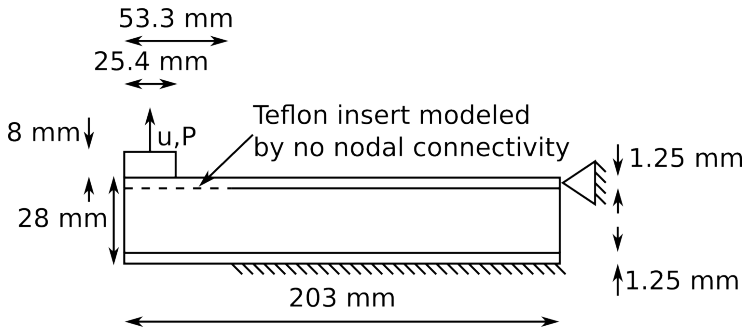

Figure 3: Schematic of the 2D finite element model including boundary conditions.

to determine the mesh convergence, insert length sensitivity, element formulation validity, etc. The schematic of the 2D model, which shows the loading and boundary conditions that are imposed on the 2D finite element model of the SCB specimen, is shown in Figure 3, and the corresponding nominal dimensions are summarized in Table 1. Only the lower half of the load introduction fixture

Table 1: Nominal dimensions in mm.

specimen length	specimen width [1]	width HiF, b [2]
200.53	25.4	23.915
facesheet thickness, t^{FS}	insert length	insert thickness
1.25	52.95	0.0001
core thickness, t^{HC}	core wall thickness	core repeating unit cell width
25.4	0.0178	4.783

[1] This width is assumed in the 2D and 3D LoF models.

[2] As outlined in this section, the model width in the HiF model has to be a multiple of the core repeating unit cell width. Thus, the HiF width varies slightly from the specimen width. A 3D LoF model with this width is also considered for the comparison of 3D HiF and 3D LoF

(see Figures 1-3) has to be modeled since the aluminum block is very rigid and the force is introduced at its center. Since there is currently no shear component in the cohesive law, a support on the right side is introduced. While shear stresses should was shown to be negligible at the interface of this mode I delamination test [51], the support is still necessary in order to prevent horizontal rigid body translations of the top facesheet.

The 3D LoF model varies from its 2D counterpart only in that it is extruded in the width direction, see Figure 4. The edges are free in the experiment as well as in the FE model, except for the bottom facesheet, which is clamped.

In contrast to the LoF model, the HiF model takes the topology of the hon-

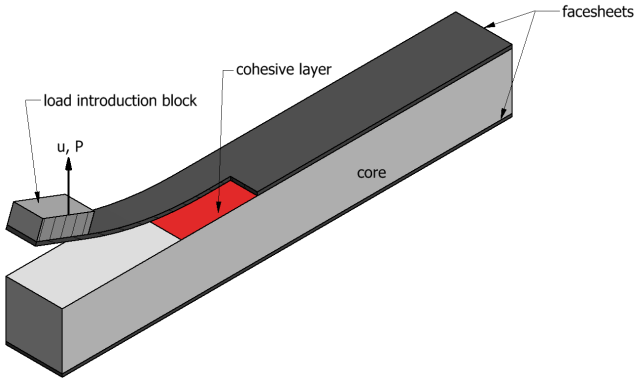

Figure 4: Schematic of the 3D low fidelity (LoF) finite element model (true to scale).

eycomb core into account. A schematic is shown in Figure 5. The nominal dimensions of the model vary slightly from the experimental dimensions in this case, as the model width currently must be a multiple of the core repeating unit cell (RUC), e.g. $5 \cdot 4.783\text{mm} = 23.915\text{mm}$, compare Table 1. The nominal dimensions are provided in Table 1, along with the nominal dimensions of the other models.

results.

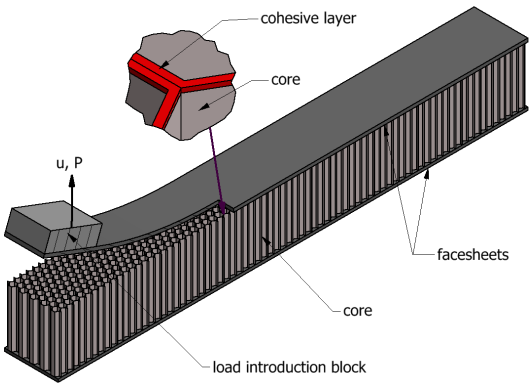

Figure 5: Schematic of the 3D high fidelity (HiF) finite element model (true to scale). Core magnification 250x.

3. Cohesive law accounting for fiber bridging

In recent work, a novel cohesive law, which accounts for fiber bridging through an initial disbond-related cohesive traction T_m and a bridging-related traction T_b, has been proposed by Höwer et al. [51, 52]. The decomposition into two distinctive cohesive mechanisms was motivated by the observation, that there are two distinct zones of high interfacial traction present in SCB experiments of CFRP facesheet / aluminum honeycomb core sandwich panels. The initial disbond-related cohesive traction T_m is observed close to the crack tip, i.e. the traction is transferred at relatively small separations. At moderate separations (e.g. 1mm) the cohesive traction value is already considerably lower than the corresponding crack tip value, see Figure 6. As the separation increases in the wake of the crack tip, the traction increases again and reaches a peak value. It can be seen clearly that the traction at high separations is transmitted through bridging fibers. At around 4-5mm, the bridging fibers break and no separation is transferred at greater separations. A cohesive law shape, which represents these observations is shown in Figure 7. The inital component is shown in red (dash-dotted line), the bridging component in green (solid line) and the resulting component in blue (dotted line).

It has been shown, that the newly proposed law provides much closer agreement

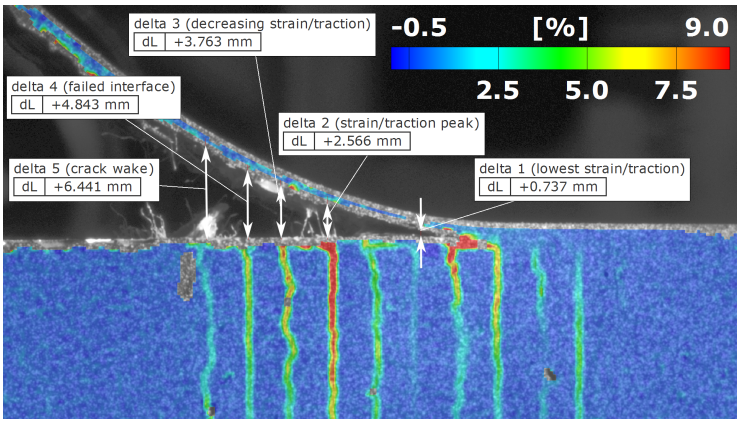

Figure 6: DIC principal strain plot with characteristic separations, cf. [51].

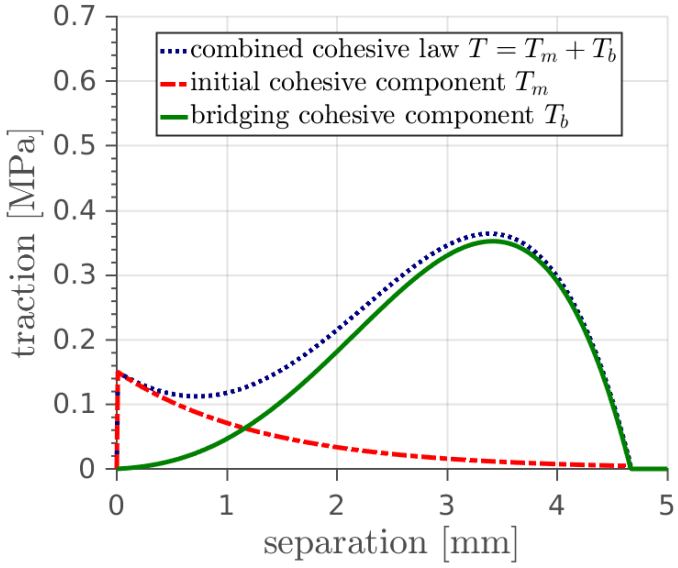

Figure 7: Traction-separation contributions of the individual cohesive components.

between predicted and measured load-displacement curves, compared to established formulations [51]. Furthermore, the newly proposed formulation is able to predict the two distinct zones of high interfacial traction, unlike previously established cohesive zone formulations. The total traction was introduced as

$$T_c(\delta_n) = T_m(\delta_n) + T_b(\delta_n) \tag{1}$$

Due to the additive split of the tractions, the total critical energy release rate (CERR) can be computed by the sum of the contributions of the two components as

$$\begin{aligned} G_{Ic} &= \int_0^{\delta^f} T(\delta_n)\,\mathrm{d}\delta_n = \int_0^{\delta^f} \left(T_m(\delta_n) + T_b(\delta_n)\right)\mathrm{d}\delta_n \\ &= \underbrace{\int_0^{\delta^f} T_m(\delta_n)\,\mathrm{d}\delta_n}_{G_{Ic,m}} + \underbrace{\int_0^{\delta^f} T_b(\delta_n)\,\mathrm{d}\delta_n}_{G_{Ic,b}} \end{aligned} \tag{2}$$

The total CERR is thus

$$G_{Ic} = G_{Ic,m} + G_{Ic,b} \tag{3}$$

The initial part of the cohesive law is chosen in a conventional way and exponential softening behavior is assumed.

$$T_m(\delta_n) = \begin{cases} T_m^{max}\frac{\delta_n}{\delta_m^0} & \text{for } \delta_n < \delta_m^0 \\ T_m^{max} e^{-\alpha\left(\delta_n/\delta_m^0 - 1\right)} & \text{for } \delta_m^0 \le \delta_n \le \delta^f \\ 0 & \text{for } \delta_n > \delta^f \end{cases} \tag{4}$$

where

$$\alpha = \frac{1}{\frac{G_{Ic,m}}{T_m^{max}\delta_m^0} - \frac{2}{3}} \tag{5}$$

holds. In Eq. (4) T_m^{max} is the maximum normal matrix/interface traction, δ_m^0 is the separation at which damage initiates.

For the bridging part, a polynomial law of the form

$$T_b(\delta_n) = \begin{cases} 0, & \text{for } \delta_n < 0 \\ C_b\left[\left(\frac{\delta_n}{\delta_b^p} + \frac{\delta_b^0}{\delta_b^p}\right)^q - \left(\frac{\delta_n}{\delta_b^p}\right)^{q+r} - \left(\frac{\delta_b^0}{\delta_b^p}\right)^q\right], & \text{for } 0 \le \delta_n \le \delta^f \\ 0, & \text{for } \delta_n > \delta^f \end{cases} \tag{6}$$

was proposed. In Eq. (6) q and r are positive numbers, δ_n is the separation, and C_b, δ_b^0 and δ_b^p are model parameters. δ^f is the separation at total failure and is not an independent parameter itself, but can be calculated from δ_b^0 and

δ_b^p. As previously, $q = 3$ and $r = 1$ were found to provide close agreement with experimental observations, and all numerical results are therefore based on this choice for the exponents. It is of note that all cohesive parameters are understood as the parameters for an element of unity width.

As the cohesive law is comprised of two superimposed cohesive components, a polynomial and an exponential one, it is denoted as Cohesive Superimposed-Polynomial-Exponential-Law (C-SPEL).

Alternatively, a simplified version of the cohesive law has also been derived in [51]. The quantities related to this formlation are denoted by hats over the respective symbols ($\hat{.}$).

$$\hat{T}_b(\delta_n) = \begin{cases} 0, & \text{for } \delta_n < 0 \\ \hat{C}_b \left[\left(\frac{\delta_n}{\hat{\delta}_b^f} \right)^{\hat{q}} - \left(\frac{\delta_n}{\hat{\delta}_b^f} \right)^{\hat{q}+\hat{r}} \right], & \text{for } 0 \leq \delta_n \leq \hat{\delta}_b^f \\ 0, & \text{for } \hat{\delta}_b^f < \delta_n \end{cases} \tag{7}$$

The initial stiffness of the alternative bridging component $\hat{T}_b$ is 0. Through the choice of appropriate cohesive parameters, the alternative formulation can be chosen very similar to T_b, except at very low separations. The latter restriction is of little importance if a pronounced T_m is present, as shown in [51]. If $\hat{T}_b$ is used $\delta_b^f = \delta^f$ holds. Thus, for $\hat{T}_b$ the failure separation is a direct model parameter. In order to avoid redundancy, the parameter transferability is shown for both formulations, but all numerical examples are based on Eq. (6). The traction-separation curves for specific parameter choices are shown in Section 6. As discussed by Höwer et al. [51, 52], it is possible to provide a physical interpretation of the model parameters by connecting the characteristic values of the cohesive law (failure separation, separation at the traction maximum, etc.) to the separation values observed in Figure 6. Some of the related analytical expressions for the characteristic values of e.g. $\hat{T}_b$ are given in Table 2.

Table 2: Material parameters of the SCB.

$\hat{T}_b$	analytical	numerical
failure separation	$\delta_b^f = \hat{\delta}_b^f$	4.67 mm
separation at highest traction	$\hat{\delta}_b^f \left(\frac{\hat{q}}{\hat{q}+\hat{r}}\right)^{1/\hat{r}}$	3.4 mm
fracture toughness $G_{Ic,b}$	$\frac{\hat{C}_b \hat{\delta}_b^f \hat{r}}{(\hat{q}+1)(\hat{q}+\hat{r}+1)}$	836 kJ/mm^2
highest traction value	$\hat{C}_b \left(\left(\frac{\hat{q}}{\hat{q}+\hat{\hat{r}}}\right)^{\hat{q}/\hat{r}} - \left(\frac{\hat{q}}{\hat{q}+\hat{r}}\right)^{(\hat{q}+\hat{r})/\hat{r}} \right)$	0.364 MPa

4. Finite element implementation

The cohesive law described in Section 3 has recently been implemented in a 2D, zero thickness, traction-separation-based Abaqus user element formulation. In this work, the formulation is extended to 3D, which is straightforward in terms of the finite element implementation.

The governing weak form is given as

$$\int_\Omega \delta\boldsymbol{\varepsilon} : \boldsymbol{\sigma}\, dV + \int_{\Gamma_c} \delta\boldsymbol{\delta} \cdot \boldsymbol{T}_c\, dS = \int_\Gamma \delta\boldsymbol{u} \cdot \boldsymbol{T}_{ext}\, dS \tag{8}$$

where Ω refers to the volume of the domain, Γ_c denotes the potential (initially internal) fracture surface and Γ denotes the external domain boundary. The strain is defined as $\boldsymbol{\varepsilon} = \nabla^{sym}\boldsymbol{u}$. By using the elasticity tensor $\boldsymbol{C}$, the stress $\boldsymbol{\sigma}$ is obtained through $\boldsymbol{\sigma} = \boldsymbol{C} : \boldsymbol{\varepsilon}$ and $\boldsymbol{T}_{ext}$ is the external traction.

Using the differential operator $\boldsymbol{B}$, which links global displacements to local separations, the internal cohesive force vector $\boldsymbol{f}_{coh}$ is given by

$$\boldsymbol{f}_{coh} = \int_{\Gamma_c} \boldsymbol{B}^T \boldsymbol{T_c} dS \tag{9}$$

which then gives rise to the element stiffness matrix

$$\boldsymbol{K}_{coh} = \frac{\partial \boldsymbol{f}_{coh}}{\partial \boldsymbol{u}} = \int_{\Gamma_c} \boldsymbol{B}^T \frac{\partial \boldsymbol{T_c}}{\partial \boldsymbol{\delta}} \boldsymbol{B}\, dS \tag{10}$$

In Eq. (10) $\boldsymbol{\delta}$ is a vector of the form $\boldsymbol{\delta} = (\delta_n, \delta_s)^T$ consisting of the normal component, δ_n,and the effective shear (tangential) component, δ_t. However, in

the present investigation, which focuses on mode I delamination, only the normal component, δ_n, is used for the calculation of cohesive tractions which leads to, $\boldsymbol{T}_c = (T_n, T_s) = (T_c, 0)$ in 2D and $\boldsymbol{T}_c = (T_n, T_{s,1}, T_{s,2}) = (T_c, 0, 0)$ in 3D. While δ_s does not enter the traction calculation, it is still used as a parameter to determine the upper bound of mode-mixity and ensure that the pure mode I assumption is justified, as shown in [51]. Since only monotonic loading is considered, no unloading condition has yet been defined.

5. Parameter transferability 2D to 3D

While the extension of the finite element implementation is very straightforward, the parameter transferability from 2D to 3D must be carefully considered. Since the 2D calculations take a fraction of the time of the 3D calculations, i.e. $\mathcal{O}(1min)$ 2D vs. $\mathcal{O}(8hrs)$ in the 3D LoF case at identical increment size and mesh density (and even much longer in the high fidelity case), it is highly desirable to establish a procedure which allows a material characterization in the 2D model and a subsequent transfer of the cohesive parameter set from the 2D model to the 3D model.

Several assumptions about the cohesive parameters have been made:

1. As the separation values of final failure and peak traction were derived from experimental DIC data, these values should remain the same in the cohesive laws of all models (2D and 3D low/high fidelity).
2. The total released energy per unit specimen width should be the same in all cases.
3. The maximum traction value of the traction-separation law should increase as the cross-sectional area of the sandwich core perpendicular to the loading direction decreases.

As a consequence of item 1 it is clear that the separation-related parameters δ_b^0 and δ_b^p should be the same in all cases. This leaves only C_b as a free parameter of T_b. As outlined in Section 2.2, two different 3D FE models are considered:

One low fidelity (LoF) model in which the core is modeled with a block-like topology and effective orthotropic material properties, see Figure 4, and one high fidelity (HiF) model, in which the core is modeled as an isotropic material with honeycomb topology, see Figure 5. In the 2D model, a computational thickness of unity is assumed. Thus, the parameters for the 2D calculation and the 3D low fidelity model should be identical, as this choice satisfies items 2 and 3. For clarity, the expression $C_b^{2D} = C_b^{3D,LoF}$ is introduced. The T_m-related cohesive parameters also do not change.

In order to ensure items 2 and 3 are also satisfied for the high fidelity case, a scaling factor λ is proposed which scales the traction separation law such that the maximum traction and CERR increase proportionally without changing the characteristic values. This can be accomplished by simply multiplying the cohesive traction with λ, i.e.

$$T_c^{HiF} = \lambda T_c^{LoF} \Rightarrow G_{I,c} = \lambda G_{I,c} \tag{11}$$

where it is proposed to choose λ as

$$\lambda = \frac{A^{3D,LoF}}{A^{3D,HiF}} \tag{12}$$

and where $A^{3D,LoF}$ and $A^{3D,HiF}$ are the cross-sectional areas perpendicular to the loading direction of the low fidelity and high fidelity models respectively, see Figure 8. In the current case, the ratio is $A^{3D,LoF}/A^{3D,HiF} = 58.306$. This increases the maximum value of T_m, T_b, $G_{I,b}$, and $G_{I,b}$ linearly. For the bridging component, where the maximum traction as well as the CERR $G_{I,b}$ is linear in C_b (Table 2), it is sufficient to scale $C_b^{3D,HiF}$ by a factor of λ

$$C_b^{3D,HiF} = \lambda C_b^{3D,LoF} = \frac{A^{3D,LoF}}{A^{3D,HiF}} C_b^{3D,LoF} \tag{13}$$

In the case of the T_m-component, both the maximum traction parameter (T_m^{max}) and the CERR parameter $G_{I,m}$ have to be scaled, i.e.

$$T_m^{3D,HiF} = \lambda T_m^{3D,LoF} \qquad G_{I,m}^{3D,HiF} = \lambda G_{I,m}^{3D,LoF} \tag{14}$$

in order to preserve the characteristic values of the cohesive law.

The three assumptions are considered valid if the load-displacement curves of the

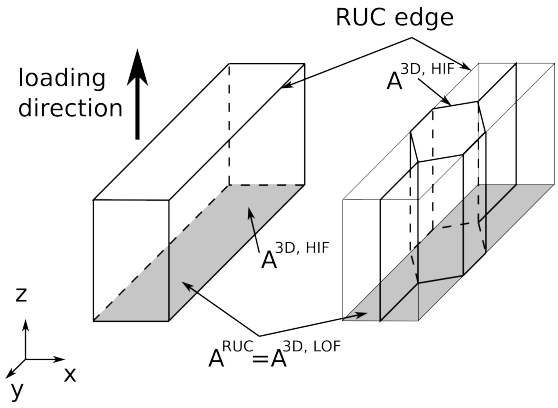

Figure 8: The effective cross-section of the low fidelity RUC (left) and the high fidelity RUC (right).

2D model under plane stress or plane strain boundary conditions are identical to the load-displacement curves of the 3D models.

The parameter transfer of the simplified model in [51] works analogously with $\hat{\delta}^{f,3D,LoF} = \hat{\delta}^{f,3D,HiF}$, $\hat{q}^{3D,LoF} = \hat{q}^{3D,HiF}$, $\hat{r}^{3D,LoF} = \hat{r}^{3D,HiF}$ and

$$\hat{C}_b^{3D,HiF} = \lambda \hat{C}_b^{3D,LoF} \tag{15}$$

An example for the scaling with a factor of $\lambda = 3$ is shown in Figure 9.

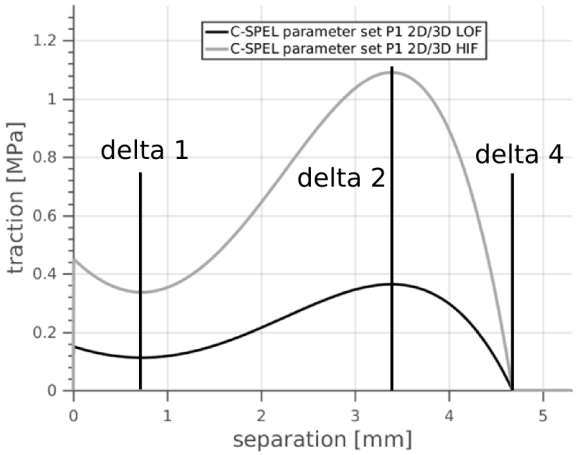

Figure 9: Example of the scaling procedure with a scaling factor of $\lambda = 3$. The characteristic values if the cohesive law remain unaffected. The delta-values are chosen in accordance with Figure 6, i.e. delta 1: lowest traction, delta 2: traction peak, delta 4: failed interface.

6. Finite element model parameters

Considerable attention has been given to the idealization of the core in order to ensure core compliance conformity between the low fidelity and high fidelity 3D models. At least in the thickness direction, which can be considered to be most crucial to the current application [22], this aim has been achieved. Thus, the shown models represent converged and robust discretizations, element formulation, and material parameter characterization. The 2D model is nearly identical to the model presented in [51]. The material parameters of the facesheets and core are given in Table 3, while the the three sets of cohesive parameters are given in Table 4. The resulting traction-separation behavior predicted by C-SPEL for the parameter sets P1 and P2 in Table 4 is shown in Figure 10.

[3] Taken from [57].

Table 3: Material parameters of the SCB.

facesheet (isotropic)		core (high fidelity)		load introduction block	
[MPa]	[−]	[MPa]	[−]	[MPa]	[−]
$E = 86,593.9$	$\nu = 0.311$	$E^{HC,HiF} = 27,550.0$	$\nu = 0.32$	$E = 72,000$	$\nu = 0.3$
facesheet (orthotropic)					
[MPa]	[MPa]	[−]	[−]	[MPa]	[MPa]
$E_{\parallel} = 86,593.9$	$E_{\perp} = 10,000.0$	$\nu_{\perp\parallel} = 0.3219$	$\nu_{\perp} = 0.024$	$G_{\perp\parallel} = 32,753.5$	$G_{\perp} = 16,379.5$
core (low fidelity)					
[MPa]	[MPa]	[−]	[−]	[MPa]	[MPa]
$E_{\parallel} = 517.1$[3]	$E_{\perp} = 0.1467$	$\nu_{\perp\parallel} = 0.33$	$\nu_{\perp} = 0.0001$	$G_{\perp\parallel} = 151.68$[3]	$G_{\perp} = 0.03669$

Table 4: Cohesive parameter sets.

cohesive parameter set P1 (LoF, plane stress fit)					
initial/matrix component			bridging component		
[MPa]	K[J/m^2]	[mm]	[MPa]	[mm]	[mm]
$T_m^{max} = 0.15$	$G_{Ic} = 0.2$	$\delta_m^0 = 0.005$	$C_b = 0.94$	$\delta_b^0 = 0.4$	$\delta_b^p = 3.65$
cohesive parameter set P2 (LoF, plane strain fit)					
initial/matrix component			bridging component		
[MPa]	[KJ/m^2]	[mm]	[MPa]	[mm]	[mm]
$T_m^{max} = 0.12$	$G_{Ic} = 0.2$	$\delta_m^0 = 0.005$	$C_b = 0.95$	$\delta_b^0 = 0.385$	$\delta_b^p = 4.1$
cohesive parameter set HiF based on parameter set P1					
initial/matrix component			bridging component		
[MPa]	[KJ/m^2]	[mm]	[MPa]	[mm]	[mm]
$T_m^{max} = 8.746$	$G_{Ic} = 11.66$	$\delta_m^0 = 0.005$	$C_b = 54.8$	$\delta_b^0 = 0.4$	$\delta_b^p = 3.65$

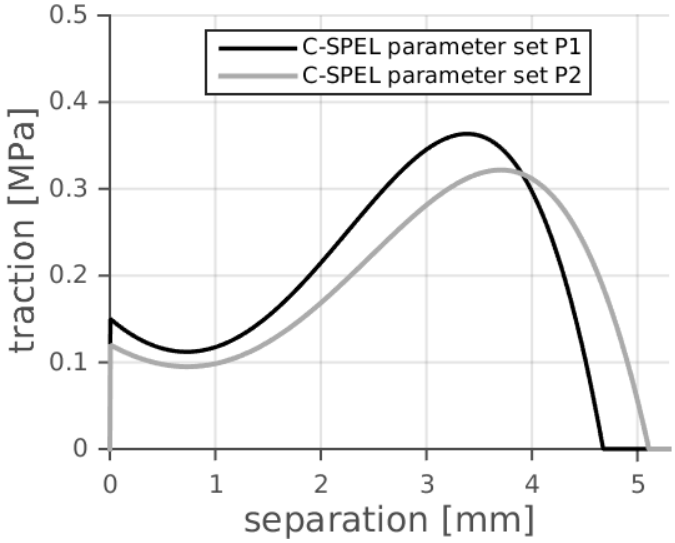

Figure 10: Traction-separation plots resulting from the cohesive parameters in Table 4.

The quasi-isotropic composite laminate facesheet has been modeled as isotropic as well as out-of-plane anisotropic/in-plane isotropic. In the isotropic case, the material parameters were chosen such that they provide the correct lever compliance. In the anisotropic case, the out-of-plane parameters were estimated based on [58, 59] and basic classical lamination theory calculations [60]. In previous investigations, the lever was considered to be isotropic and the assumption was found to have no influence in the 2D case. Both cases were considered separately, in order to investigate if there is an influence in the 3D case. In accordance with the corresponding literature [16–18], no influence of the out-of-plane thickness on the load-displacement or R-curves was found. Thus, the current results are comparable to previous results, cf. [51, 52]. The LoF core was modeled as anisotropic due to the great disparity in Young's moduli in through-thickness and in-plane directions. The HiF core material is modeled as isotropic, as experiments on the foil material showed that the axial and transverse Young's moduli varied by only 0.24% with a standard deviation of 2.18% of the meassured value. A knockdown factor is applied to the meassured Young's model such that the behavior of a unit cell, as shown in Figure 8, corresponds to the meassured value in flatwise tension. The knockdown factor includes the effects of e.g. geometrical imperfections. For the facesheets, core, and load introduction block Abaqus reduced integration standard elements were used, see Table 5. The cohesive layer was modeled with cohesive user elements. A mesh refinement study was conducted in longitudinal direction to ensure sufficiently refined crack propagation results.

Table 5: Discretization and element formulation details for the models.

model	solid element type	total # elements	total # nodes
2D plane strain	CPE4R	7,294	7,596
2D plane stress	CPS4R	7,294	7,596
3D plane stress/strain	CPS4R	7,294	15,192
3D low fidelity (width=25.4 mm)	C3D8R	176,300	191,621
3D low fidelity (width=23.915 mm)	C3D8R	167,568	182,451
3D high fidelity	C3D8R	2,499,660	3,394,961

7. Results and discussion

The results and discussion section is split into four main parts: 1.) load-displacement results and discussion for various models, 2.) curvature of the delamination front 3.) presentation of R-curve results, comparison, and discussion, and 4.) mode partitioning and concluding remarks.

7.1. Comparison of load-displacement curves

7.1.1. Comparison of 2D plane stress to 3D low fidelity load-displacement curves

After verifying that the 3D element formulation gives the same answer for the same boundary value problem (plane stress), it is investigated if the cohesive parameters, which were obtained by fitting the 2D plane stress model to the experimental results, can be transferred to the full 3D low fidelity prediction with the same paramter set P1 (C-SPEL full 3D LoF P1). As shown in Figure 11, nearly exact agreement between the 2D plane stress and the full 3D LoF model is achieved and no refitting of model parameters is necessary. Thus, the plane stress boundary condition provides a suitable approximation of the coupon level experiment.

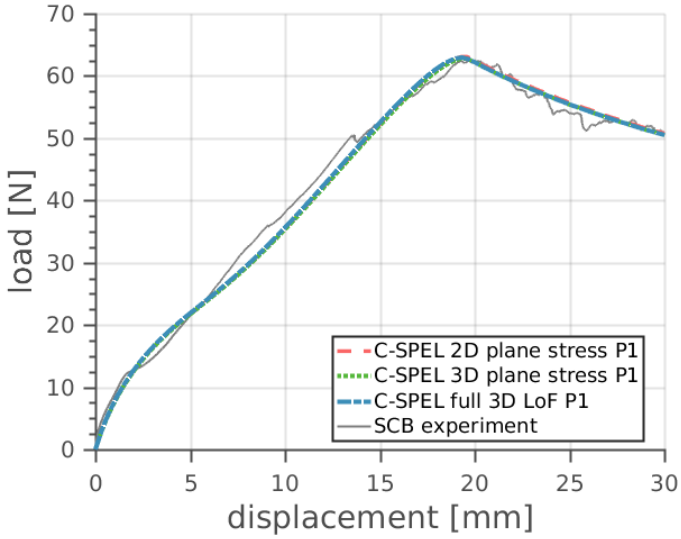

Figure 11: Comparison of the 2D plane plane stress prediction to the equivalent 3D boundary condition prediction and the full 3D prediction.

7.1.2. Comparison of 2D plane strain to 3D low fidelity load-displacement curves

As shown in Figure 12, when cohesive parameter set P1, which provided a good fit to experimental data for 2D plane stress and conditions, is used in the plane strain case, the predicted load-displacement curve deviates from experimental results, as expected. The peak load difference is 4.87%. Therefore, the parameters are re-fit for the plane strain case, leading to cohesive parameter set P2, shown in Table 4. Cohesive parameter set P2 provides a good fit to experimental data under plane strain assumptions, see Figure 12. However, when cohesive parameter set P2 is used in the 3D low fidelity model, there is disagreement between the 2D plane strain and 3D predictions and consequently with experimental results, see Figure 12. The peak load difference is 3.77% in this case. Thus, in the case of the mode I disbonding of a CFRP facesheet from an aluminum honeycomb core sandwich the plane stress assumption seems to be valid. The debate on the appropriateness of plane strain and plane stress assumptions in monolithic laminates [16–18] and the common application of both

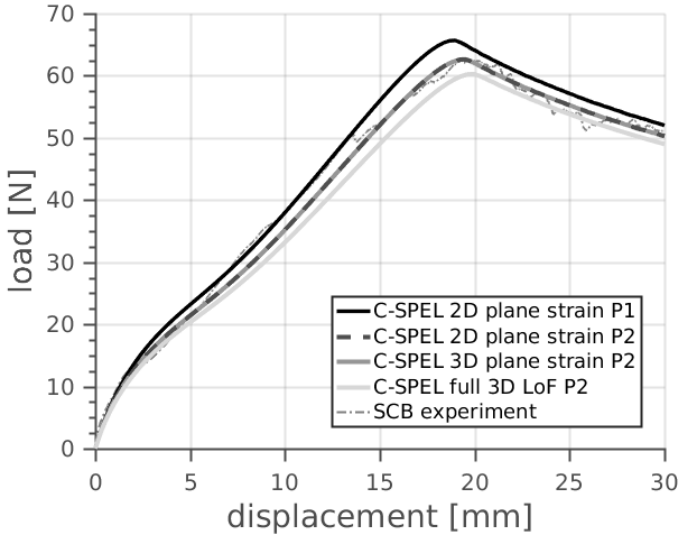

Figure 12: Comparison of the 2D plane strain predictions to equivalent 3D boundary conditions.

plane strain [53, 54] as well as plane stress assumptions [55, 56] may indicate that other geomtries or core materials could potentially affect the validity of the in-plane assumptions.

7.1.3. Comparison of 3D low fidelity to 3D high fidelity load-displacement curves

In Section 7.1.1 it was shown that the 2D plane stress and 3D LoF predictions are in excellent agreement with the experimental results when the specimen width and the model width is identical. Unfortunately, the direct comparison of the HiF computation to experiments is not currently feasible, as the developed honeycomb geometry generation algorithm requires the specimen width to be multiples of one honeycomb unit cell width as outlined in Section 2.2. Thus, the exact test specimen width cannot be matched in the HiF case. Therefore, the HiF predictions have been compared to LoF predictions of identical specimen width in this section. As the LoF model was already shown to be in excellent agreement with experiments, this procedure should be valid.

Figure 13 shows that the 3D LoF and 3D HiF predictions are all in excellent agreement. This therefore validates the proposed parameter transfer procedure. A parameter study in which the in-plane Young's modulus of the homogenized

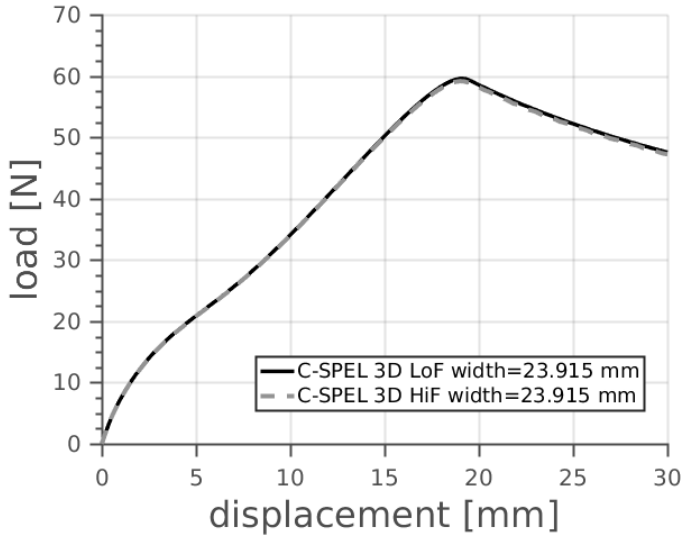

Figure 13: Comparison of 3D LoF to 3D HiF load-displacement results.

core material is varied confirms that the load-displacement curve is insensitive with respect to the in-plane Young's modulus of the homogenized core material.

7.1.4. Load-displacement curves - conclusion

Sections 7.1.1-7.1.3 clearly demonstrate that, for a characterization of the material interface, only 2D plane stress calculations have to be performed. This is a great benefit, since it is possible to carry out several hundred 2D calculations on a personal computer in less than an hour, which is unrealistic even for the LoF 3D calculations not to mention the 3D HiF calculation. This is a very important factor, since the simulation must be run multiple times in the parameter fitting stage, but only once on the structural level (without parallelization, 2D: $\mathcal{O}$(1min), 3D LoF: $\mathcal{O}$(8hrs), 3D HiF: $\mathcal{O}$(3weeks)). The in-plane constrained modulus of the core was found to have negligible effect, as well as the out-of-plane anisotropy of the facesheet.

7.2. Curvature of the delamination front

The curvature of the delamination front is a well-known aspect of DCB and SCB tests which is caused by anticlastic bending [16, 18]. The shape of the delamination front is often described as "thumbnail-shaped" [15, 17]. The thumbnail-shaped curvature of the crack front was also present in the current 3D simulation results. The contour of the crack front predicted by the currently used crack length criterion ([52], Section 7.3) is shown in Figure 14. A relative

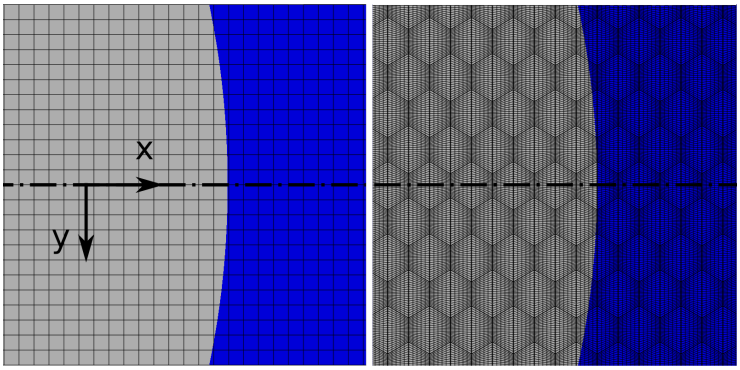

Figure 14: Fully developed crack front contours of the LoF (left) and HiF (right) models (width of 23.915 mm). The element edge length is approximately 1 mm in the LoF model.

metric for the severity of the crack front curvature can be defined as

$$\Delta\hat{a}_{\mathrm{curv}} = \frac{\Delta a|_{y=0} - \Delta a|_{y=\pm b/2}}{b} \tag{16}$$

i.e. the difference in crack length at the centerline and the crack length at the edge normalized over the specimen width. The quantities for the LoF and HiF case with a width of 23.915 mm are plotted in Figure 15. The difference between the crack propagation on the surface and at the centerline increases initially until a saturation value is reached after 15-20 mm of crack propagation. This corresponds to the peak load which coincides with the full formation of the fracture zone / bridging mechanism. The difference in crack length is about 1.3 mm, i.e. 5-6% of the width, and there is no pronounced difference between the LoF and HiF case, see Figure 15. The read-off accurracy was 0.1mm, which explains some of the existing scatter.

It is of note that, the locus of the highest normal stress points close to the

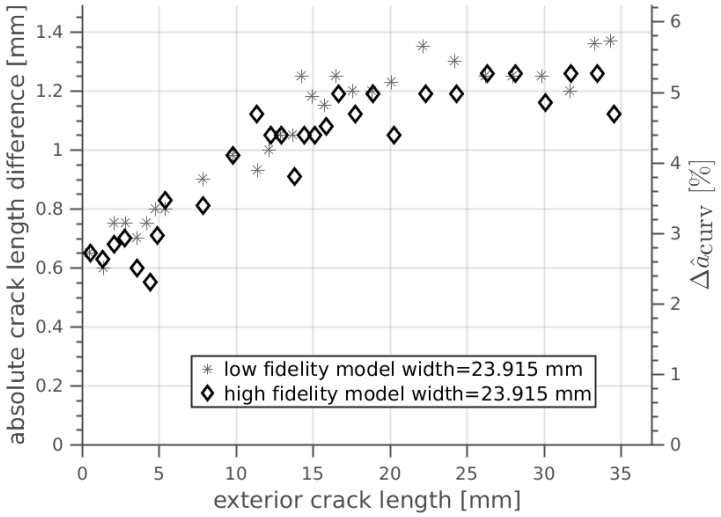

Figure 15: Comparison between the HiF and LoF model in terms of crack curvature, defined as the variation between the centerline crack growth and the surface crack growth. Both ordinates are valid for all points.

crack front has a more pronounced curvature than the curvature of the crack front under the currently used crack criterion, see Figure 16. The model predicts a pronounced thumbnail shape of the apparent crack front (Figure 14) as well as for the locus of highest thickness-direction normal stress $S33$ (Figure 16) points, which is associated with the T_m-related crack front. However, the bridging-related (T_b) locus of the highest $S33$ values is essentially a straight line, see Figure 22. The reason for this curvature difference between the stress fronts is that the curvature is driven by anticlastic bending. The anticlastic bending-induced variation in vertical displacement across the width at a given longitudinal position is very small, i.e. only a fraction of a millimeter. However, the T_m-component of the present cohesive formulation is very sensitive with respect to these minor variations in displacement at low separation values. At larger separations, i.e. in the bridging-dominated (T_b) domain of the cohesive law, the slope of the traction-separation law is comparatively low and minor

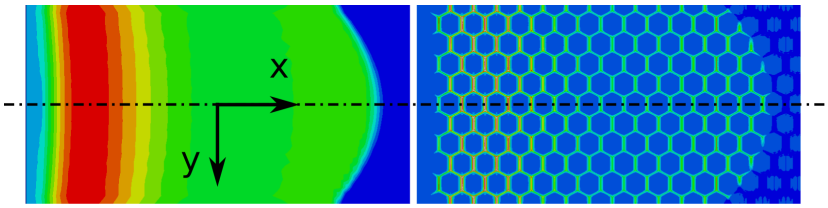

Figure 16: Comparison between the HiF (left) and LoF (right) model the thickness direction normal stresses in the facesheet above the cohesive layer (S33). The two contour plots have been plotted with approximately scaled stress ranges for emphasis.

displacement variations due to anticlastic bending do not manifest in noticeable changes in cohesive traction or core strain. Thus, the minor saddle-shaped deflection shape, which is also present in the wake of the crack tip, causes a considerably lower curvature of the $S33$ peak locus in the bridging-dominated domain.

7.3. Comparison of R-curves

Another important meassure of the accuracy of the numerical predictions, besides the comparison of measured and predicted load-displacement curves, are the measured and predicted R-curves.

To this end, a dissipation, threshold-based, engineering estimate for the comparison of FE-predicted R-curves and experimental R-curves has been proposed and verified in [52]. The method assumes that a crack is visible in the experiment once a certain dissipated energy level $\theta_{Ic,m}$ of the matrix-related component has been reached. This fraction $\theta_{Ic,m}$ is defined as

$$\theta_{Ic,m} = \frac{G_{I,\text{crack tip}}}{G_{Ic,m}} \tag{17}$$

Thus, it is assumed that $\theta_{Ic,m}$ is the fraction of the matrix-related CERR which needs to be dissipated before a visible crack propagation can occur. From the dissipated energy level, $\theta_{Ic,m}$, a corresponding opening, δ_θ, is calculated from

$$G_{I,\text{crack tip}} = \theta_{Ic,m} G_{Ic,m} = \int_0^{\delta_\theta} T_m(\delta_n)\,\mathrm{d}\delta_n \tag{18}$$

During postprocessing, the longitudinal position at which the specific opening value δ_θ is met is extracted from the FE output, and the apparent CERR, according to Eq. (19), is calculated using the associated load and displacement values. For the 3D predictions, this process is carried out at the centerline ("mid") as well as on the surface ("ext") of the specimen. Once the load point displacement u, load P, and crack length Δa is known, the apparent fracture toughness, according to ASTM D 5528, can be estimated as

$$G_{Ic,\mathrm{ASTM}} = \frac{3Pu}{2b(a_0 + \Delta a)} \tag{19}$$

The resulting R-curves for the 2D plane stress and 3D LoF cases are shown in Figure 17. It can be seen, that the 2D plane stress curve is between the cen-

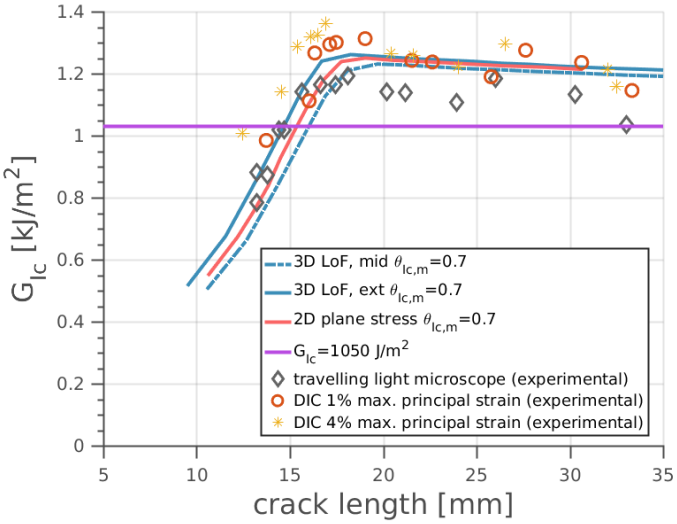

Figure 17: Comparison 2D and 3D low fidelity (LoF) R-curve predictions to experimental results. $\theta_{Ic,m} = 0.7$ in all computations.

terline curve (mid) and the surface (ext) curve. The best agreement between experiments and numerical predictions is observed for the surface (ext) curve, which is desirable as this is the quantity that was measured in the experiment. In the literature, it is observed that the laminate layup has an influence on

the curvature of the delamination front and thus on the apparent R-curve [15, 16, 18]. In the current investigation no difference is observed between the orthotropic and the isotropic case. While unintuitive, this observation is in agreement with the refrences mentioned above, as the currently investigated specimen is in-plane isotropic, and the literature suggests that the R-curve dependence is mostly driven by

$$D_c = \frac{D_{12}^2}{D_{11} D_{22}} \tag{20}$$

where D_{12}, D_{11}, and D_{22} are the flexural rigidities [15, 16, 18]. This means that the out-of-plane modulus should not affect the results. Indeed, the out-of-plane orthotropy is confirmed to have negligible influence on the R-curve by using isotropic and out-of-plane anisotropic material parameters according to Table 3.

A comparison between the 3D LoF and 3D HiF R-curve predictions is shown in Figure 18. While Figure 15 indicates that the difference between centerline and

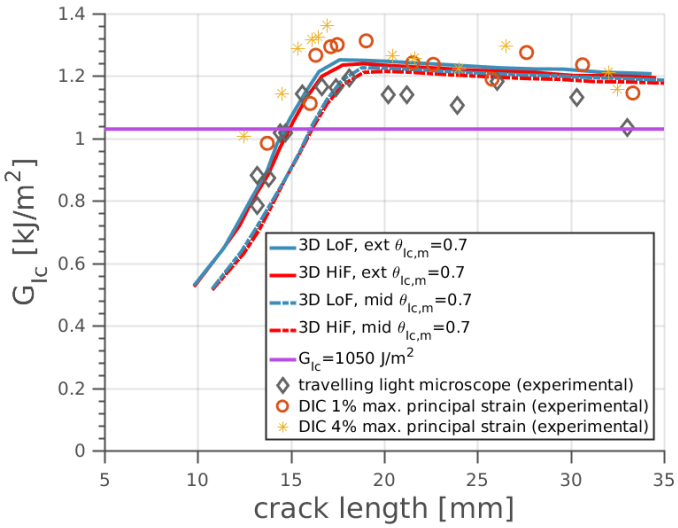

Figure 18: Comparison 3D low fidelity (LoF) and 3D high fidelity (HiF) R-curve predictions to experimental results. $\theta_{Ic,m} = 0.7$ in all computations.

surface crack length remains constant after a saturation value has been reached,

the centerline and surface R-curves converge to the same value, which is easily explained through Eq. (19). While the absolute difference Δa remains constant, the relative difference decreases and thus the R-curves converge at higher crack lengths values.

In conclusion, the numerical R-curve predictions and the experimentally measured R-curves are in close agreement. The numerical model predicts different R-curves for the centerline of the specimen and the edge of the specimen, due to the curvature of the delamination front. As expected, the R-curve which is predicted at the edge of the specimen shows the closest agreement with the experimental results. The R-curve predictions of the LoF and HiF model at a given specimen width are in very close agreement. Thus the crack growth and energy dissipation is well-captured by the proposed model.

7.4. Mixed mode partitioning and concluding remarks

The predictions of the load-displacement curves and R-curves between for the HiF and LoF models match almost surprisingly well. Furthermore, it seems almost unintuitive that the SCB sandwich panel is in a state of almost pure mode I delamination [51], when the SCB test for monolithic laminates is often reported to have a mode mixity of approximately $G_I/G \approx 63\%$ [61]. The reason for both observations is likely the orthotropy, and especially the low in-plane stiffness, of the honeycomb core. The in-plane Young's modulus of the honeycomb core is $E_{\perp}^{HC} = 0.1467\,\mathrm{MPa}$ while the in-plane Young's modulus of the facesheet $E_{\parallel}^{FS} = 86,593,9\,\mathrm{MPa}$ is about five orders of magnitude higher. Note that $E_{\parallel}^{FS}$ denotes the in-plane modulus of the in-plane isotropic laminate, i.e. there is no preferred fiber direction in-plane and there is no distinction between individual layers. The high difference in stiffness leads to a significant difference in the magnitude of the in-plane normal stresses in the facesheet and the core, namely five orders of magnitude, see Figure 19. Since the in-plane normal stresses in the core are approximately 0 and there is negligible honeycomb core curvature, $\frac{\mathrm{d}\phi^{HC}}{\mathrm{d}x}$, it can be assumed that the transferred moment in the core, M^{HC}, where

$$M^{HC} = E^{HC} I^{HC} \frac{\mathrm{d}\phi^{HC}}{\mathrm{d}x} \approx 0 \tag{21}$$

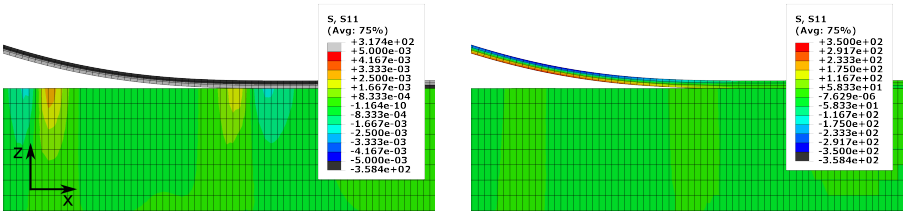

(a) Longitudinal normal stress contour plot ranging from -0.005 MPa to 0.005 MPa (normal stress level in the core).

(b) Longitudinal normal stress contour plot ranging from -350 MPa to 350 MPa (normal stress level in the facesheet).

Figure 19: Longitudinal normal stresses close to the crack tip.

is also approximately zero. In Eq. (21) I^{HC} denotes the second moment of area defined through

$$I^{HC} = \frac{b{t^{HC}}^3}{12} \tag{22}$$

where b and t^{HC} are given in Table 1. A schematic adopted from Williams [61] and modified for the current purpose is shown in Figure 20. The clamped bottom facesheet is treated as a solid foundation.

Starting from the basic definition of the energy release rate G

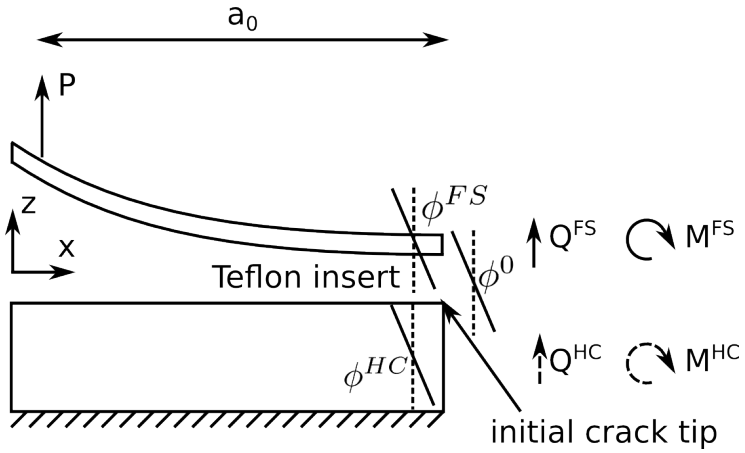

Figure 20: Schematic of the forces and moments close to the crack tip prior to crack propagation.

$$G = \frac{1}{b}\left(\frac{\mathrm{d}U_e}{\mathrm{d}a} - \frac{\mathrm{d}U_s}{\mathrm{d}a}\right) \tag{23}$$

where U_e the external work performed and U_s is the strain energy an estimate for the mode-mixity (mode partitioning) is derived.

In the current case it is quickly shown that the moments initially cause no net external or net internal work when, besides $M^{HC} \approx 0$ (Eq. (21)), it is assumed that the bending stiffness of the honeycomb K^{HC} is approximately 0 and thus

$$K^{HC} = E^{HC} I^{HC} \approx 0 \qquad \text{and} \qquad K^0 \approx K^{FS} \tag{24}$$

where K^0 denotes the bending stiffness of the bonded core and top facesheet. While the argument for neglecting the bending moment in the core was based on a difference of five orders of magnitude for the relevant longitudinal stresses, the difference in bending stiffness between the core and the facesheet is, due to the much hicher core thickness only

$$\frac{K^{FS}}{K^{HC}} = 70.35 \tag{25}$$

The difference is considered to be sufficiently high to be neglected . It then follows that

$$\frac{\mathrm{d}\phi^{FS}}{\mathrm{d}a} = \frac{M^{FS}}{E^{FS} I^{FS}} \qquad \text{and} \qquad \frac{\mathrm{d}\phi^{0}}{\mathrm{d}a} = \frac{M^{FS} + M^{HC}}{E^{0} I^{0}} \approx \frac{M^{FS}}{E^{FS} I^{FS}} \tag{26}$$

Using this approximation, the external work is clearly zero since

$$\delta U_e = M^{FS}\left(\underbrace{\frac{\mathrm{d}\phi^{HC}}{\mathrm{d}a} - \frac{\mathrm{d}\phi^{0}}{\mathrm{d}a}}_{\approx 0}\right)\delta a + \underbrace{M^{HC}}_{\approx 0}\left(\frac{\mathrm{d}\phi^{HC}}{\mathrm{d}a} - \frac{\mathrm{d}\phi^{0}}{\mathrm{d}a}\right)\delta a \approx 0 \tag{27}$$

Similarly, the net strain energy contribution of the moments is zero under the described approximations

$$\begin{aligned} \delta U_s &= \frac{{M^{FS}}^2}{2E^{FS} I^{FS}} + \frac{{M^{HC}}^2}{2E^{HC} I^{HC}} - \frac{\left(M^{HC} + M^{FS}\right)^2}{2E^{0} I^{0}} \\ &\approx \frac{{M^{FS}}^2}{2E^{FS} I^{FS}} - \frac{{M^{FS}}^2}{2E^{FS} I^{FS}} = 0 \end{aligned} \tag{28}$$

Thus, only the contribution of the shear forces Q^{FS} and Q^{HC} remains. From the free body diagram Q^{HC} is clearly 0 at the onset of crack propagation, as

there are no tractions across the insert. As shown by Williams [61] the shear forces only contribute towards mode I delamination and the contribution can be calculated as

$$\tau = \frac{3}{2}\left(\frac{Q^{FS}}{bt^{FS}}\right)\left(1 - \frac{z^2}{\left(t^{FS}/2\right)^2}\right) \tag{29}$$

where τ is the shear stress in the facesheet. The facesheet is considered isotropic and possible shear variations across the thickness due to the layup are neglected. Using Eq. (29), and exploiting that

$$\int_0^{t^{FS}/2}\left(1 - \frac{z^2}{(t^{FS}/2)^2}\right)^2 \mathrm{d}z = \frac{4t^{FS}}{15} \tag{30}$$

the shear force contribution towards the strain energy can be expressed as

$$\frac{\mathrm{d}U_s}{\mathrm{d}a} = 2B\int_0^{t^{FS}/2}\frac{1+\nu_\perp^{FS}}{E^{FS}}\tau^2\,\mathrm{d}z = \frac{6}{5}\frac{1+\nu_\perp^{FS}}{E^{FS}}\frac{{Q^{FS}}^2}{bt^{FS}} \tag{31}$$

which leads to

$$G_I = \frac{3}{5}\frac{1+\nu_\perp^{FS}}{E^{FS}}\frac{{Q^{FS}}^2}{bt^{FS}} \qquad \text{and} \qquad G_{II} = 0 \tag{32}$$

The validity of the assumptions is checked by computing the R-curve from Eq. (32). The results is shown in Figure 21 and very close agreement between the analytical prediction and e.g. the centerline R-curve of the 3D model is observed up to approximately 16 mm crack length. The deviation becomes noticeable at approximately Stage III of crack formation as identified by Höwer et al. [51], i.e. the stage at which the the fiber bridging becomes clearly noticeable. In the free body diagram shown in Figure 20, on which the derivation is based, a traction-free surface in the wake of the crack tip, and more specifically across the Teflon insert, is assumed. The assumption of a traction free-surface is cleraly violated when the length of the process zone is ca. 20 mm and the insert length $a_0 = 52.95$ mm is less then 3 times the process zone length, especially when the highest tractions occur far in the wake of the crack, as is the case in the proposed model. Thus, the traction in the wake of the crack tip would have to be included in the calculation of G if the prediction is to be valid for propagating crack. However, the presence of cohesive normal tractions will not

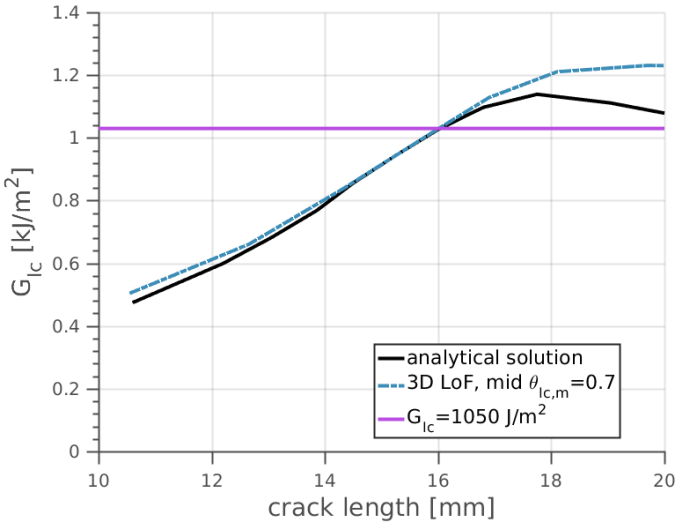

Figure 21: Comparison of the analytical R-curve prediction based on Eq. (32) the apparent R-curve extracted from FE predictions. The FE R-curve identical to the curve shown in Figure 17.

lead to any mode II contribution. Thus, the crack propagation was shown to be clearly mode I dominated and the made assumptions seem to be justified in this case. Naturally, the estimate is very crude and could be refined in many regards [62–66].

The high in-plane compliance of the core, compared to the out of plane compliance, in the LoF as well as the HiF models, also ensures that there are only negligible in-plane normal stresses (S11, S22) and that the gradient of the out of plane normal stress (S33) is very small in both cases, see Figure 22. This separation of the in-plane and out of plane stresses probably contributes significantly to the very close agreement between LoF and HiF load-displacement curves despite the vastly different core topologies and and cohesive strength values.

Lastly, it should be mentioned that there were noticeable shear stresses several mm beneath the interface in the HiF model, even when there was no tangential traction at the interface. These shear stresses were not present in the LoF model

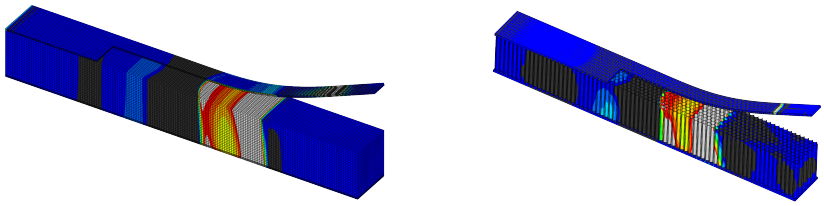

(a) Normal stress in thickness direction of the 3D LoF model width=(23.915 mm) at $\Delta a \approx 20\,mm$.

(b) Normal stress in thickness direction of the 3D HiF model (width=23.915 mm) at $\Delta a \approx 20\,mm$.

Figure 22: Thickness direction normal stress ($S33$) contour plots of the HiF and LoF predictions.

and are thus likely caused by the honeycomb topology of the core. While these stresses were shown to have no influence on the global load-displacement curves, the observed shear stresses may facilitate the crack propagation into the core.

8. Conclusion

A recently proposed cohesive zone formulation, which accounts for fiber bridging in a novel way, has been extended from 2D to 3D. The SCB specimen was shown to be closer to a state of plane stress, as there was excellent agreement between 2D plane stress and 3D models of high and low fidelity, but not between 2D plane strain and 3D models of identical material and cohesive parameters. This comparison also showed that 3D effects had negligible influence on the load-displacement curves. Thus, the characterization of the cohesive interface parameters can be accomplished with very efficient 2D plane stress simulations, which require less than a minute of calculation time each. This is a great benefit, as the 2D model may have to be run multiple times for fitting purposes, but the 3D structural calculation only has to be run once. The 3D low fidelity and 3D high fidelity models showed excellent agreement in terms of the load-displacement curves and R-curves. Therefore, it is recommended to use a low fidelity 3D model for structural applications, as the computational

time is significantly lower, while the same accuracy is achieved in terms of the facesheet to core delamination, when the newly proposed cohesive formulation is used. Lastly, an estimate of the mode mixity of the SCB is provided.

Acknowledgments

The authors are thankful for insightful discussions concerning the mixed-mode partitioning of laminates with C.M. Harvey and S.Wang. The first author acknowledges support from the Excellence Initiative of the German federal and state governments. E. J. Pineda acknowledges funding through the von Kármán fellowship GS069 and the Alexander von Humboldt Foundation. Funding by the Ministry of Innovation, Science and Research of the State of North Rhine-Westphalia is acknowledged by J.-W. Simon. The NASA authors acknowledge the Space Launch System (SLS) program for their support.

[1] K. S. Raju, B. L. Smith, J. S. Tomblin, K. S. Liew, J. C. Guarddon, Impact damage resistance and tolerance of honeycomb core sandwich panels, Journal of Composite Materials 42 (2008) 385–412.

[2] T. S. McQuigg, R. K. Kapania, S. J. Scotti, S. P. Walker, Compression after impact on honeycomb core sandwich panels with thin facesheets, part 1: Experiments, in: 53rd AIAA/ASME/ASCE/AHS/ASC Structures, Structural Dynamics, and Materials Conference, 2012.

[3] J. G. Ratcliffe, W. C. Jackson, A finite element analysis for predicting the residual compressive strength of impact-damaged sandwich panels, NASA/TM-2008-215341.

[4] T. E. Lacy, Y. Hwang, Numerical modeling of impact-damaged sandwich composites subjected to compression-after-impact loading, Composite Structures 61 (2003) 115–128.

[5] A. Hodge, A. Nettles, J. Jackson, Comparison of open-hole compression strength and compression after impact strength on carbon fiber/epoxy laminates for the Ares I composite interstage, NASA/TP-2011-216460.

[6] T. McQuigg, Compression after impact experiments and analysis on honeycomb core sandwich panels with thin facesheets, NASA/CR-2011-217157.

[7] B. Zalewski, B. Bednarcyk, ACT payload shroud structural concept analysis and optimization, NASA/TM-2010-216942.

[8] E. Pineda, D. Myers, D. Kosareo, B. Zalewski, G. Dixon, Buckling testing and analysis of honeycomb sandwich panel arc segments of a full-scale fairing barrel part 2: 6-ply in-autoclave facesheets, NASA/TM-2013-217822/PART2.

[9] E. Pineda, D. Myers, D. Kasareo, S. Kellas, Buckling testing and analysis of honeycomb sandwich panel arc segments of a full-scale fairing barrel part 3: 8-ply out-of-autoclave facesheets, NASA/TM-2014-217822/PART3.

[10] N. Pagano, G. Schoeppner, Delamination of polymer matrix composites: problems and assessment, Comprehensive composite materials 2 (2000) 433–528.

[11] C. Sarrado, A. Turon, J. Renart, I. Urresti, Assessment of energy dissipation during mixed-mode delamination growth using cohesive zone models, Composites Part A: Applied Science and Manufacturing 43 (2012) 2128–2136.

[12] M. Somers, T. Weller, H. Abramovich, Buckling and postbuckling behavior of delaminated sandwich beams, Composite Structures 21 (1992) 211–232.

[13] T.-S. Han, A. Ural, C.-S. Chen, A. Zehnder, A. Ingraffea, S. Billington, Delamination buckling and propagation analysis of honeycomb panels using a cohesive element approach, International Journal of Fracture 115 (2002) 101–123.

[14] ASTM D 5528, Standard test method for mode I interlaminar fracture toughness of unidirectional fiber-reinforced polymer matrix composites, ASTM International (2007).

[15] M. Shokrieh, M. Heidari-Rarani, S. Rahimi, Influence of curved delamination front on toughness of multidirectional DCB specimens, Composite Structures 94 (2012) 1359–1365.

[16] B. D. Davidson, R. A. Schapery, Effect of finite width on deflection and energy release rate of an orthotropic double cantilever specimen, Journal of Composite Materials 22 (1988) 640–656.

[17] B. D. Davidson, An analytical investigation of delamination front curvature in double cantilever beam specimens, Journal of Composite Materials 24 (1990) 1124–1137.

[18] B. D. Davidson, R. A. Schapery, A technique for predicting mode I energy release rates using a first-order shear deformable plate theory, Engineering Fracture Mechanics 36 (1990) 157–165.

[19] J. Reiner, J. P. Torres, M. Veidt, A novel top surface analysis method for mode i interface characterisation using digital image correlation, Engineering Fracture Mechanics 173 (2017) 107–117.

[20] B. Krull, J. Patrick, K. Hart, S. White, N. Sottos, Automatic optical crack tracking for double cantilever beam specimens, Experimental Techniques (2015) 1–9.

[21] D. Adams, J. Nelson, Z. Bluth, C. Hansen, Development and evaluation of fracture mechanics test methods for sandwich composites, in: Proc. FAA JAMS Tech. Rev. Meet. Wichita, KS, 2010.

[22] J. G. Ratcliffe, J. R. Reeder, Sizing a single cantilever beam specimen for characterizing facesheet-core debonding in sandwich structure, Journal of Composite Materials 45 (2011) 2669–2684.

[23] M. Rinker, J. G. Ratcliffe, D. O. Adams, R. Krueger, Characterizing facesheet/core disbonding in honeycomb core sandwich structure, NASA/CR-2013-217959 NIA Report No. 2013-0115 (2013) 1–35.

[24] M. Rinker, R. Krueger, J. Ratcliffe, Analysis of an aircraft honeycomb sandwich panel with circular face sheet/core disbond subjected to ground-air pressurization, NASA/CR-2013-217974 2013-0116 (2013) 1–27.

[25] A. Ural, A. Zehnder, A. Ingraffea, Fracture mechanics approach to facesheet delamination in honeycomb: measurement of energy release rate of the adhesive bond, Engineering Fracture Mechanics 70 (2003) 93–103.

[26] K. N. Shivakumar, S. Smith, In situ fracture toughness testing of core materials in sandwich panels, Journal of Composite Materials 38 (2004) 655–668.

[27] K. N. Shivakumar, H. Chen, S. Smith, An evaluation of data reduction methods for opening mode fracture toughness of sandwich panels, Journal of Sandwich Structures & Materials 7 (2005) 77–90.

[28] S.-D. Pan, L.-Z. Wu, Y.-G. Sun, Z.-G. Zhou, Fracture test for double cantilever beam of honeycomb sandwich panels, Material Letters 62 (2008) 523–526.

[29] P. P. Camanho, C. G. Dávila, M. F. de Moura, Numerical simulation of mixed-mode progressive delamination in composite materials, Journal of Composite Materials 37 (2003) 1415–1438.

[30] A. Turon, P. Camanho, J. Costa, C. Dávila, A damage model for the simulation of delamination in advanced composites under variable-mode loading, Mechanics of Materials 38 (2006) 1072–1089.

[31] S. Li, M. Thouless, A. Waas, J. Schroeder, P. Zavattieri, Use of mode-I cohesive-zone models to describe the fracture of an adhesively-bonded polymer-matrix composite, Composites Science and Technology 65 (2005) 281–293.

[32] S. Li, M. Thouless, A. Waas, J. Schroeder, P. Zavattieri, Use of a cohesive-zone model to analyze the fracture of a fiber-reinforced polymer-matrix composite, Composites Science and Technology 65 (2005) 537–549.

[33] S. Li, M. Thouless, A. Waas, J. Schroeder, P. Zavattieri, Mixed-mode cohesive-zone models for fracture of an adhesively bonded polymer-matrix composite, Engineering Fracture Mechanics 73 (2006) 64–78.

[34] C. G. Dávila, C. A. Rose, P. Camanho, A procedure for superposing linear cohesive laws to represent multiple damage mechanisms in the fracture of composites, International Journal of Fracture 158 (2009) 211–223.

[35] A. Airoldi, C. G. Dávila, Identification of material parameters for modelling delamination in the presence of fibre bridging, Composite Structures 94 (11) (2012) 3240–3249.

[36] R. Gutkin, M. Laffan, S. Pinho, P. Robinson, P. Curtis, Modelling the R-curve effect and its specimen-dependence, International Journal of Solids and Structures 48 (2011) 1767–1777.

[37] S. El-Sayed, S. Sridharan, Predicting and tracking interlaminar crack growth in composites using a cohesive layer model, Composites Part B: Engineering 32 (6) (2001) 545–553.

[38] B. F. Sørensen, T. K. Jacobsen, Large-scale bridging in composites: R-curves and bridging laws, Composites Part A 29A (1998) 1443–1451.

[39] X. Lu, J. Teng, L. Ye, J. Jiang, Bond-slip models for sheets/plates bonded to concrete, Engineering Structures 27 (2005) 938–950.

[40] K. W. Neale, U. A. Ebead, H. M. A. Baky, W. E. Elsayed, A. Godat, Analysis of the load-deformation behaviour and debonding for FRP-strengthened concrete structures, Advances in Structural Engineering 9 (2006) 751–763.

[41] S. Feih, Development of a user element in abaqus for modelling of cohesive laws in composite structures, Risø-R Report 1501(EN) (2005) 1–52.

[42] K. Park, G. H. Paulino, Computational implementation of the ppr potential-based cohesive model in abaqus: Educational perspective, Engineering Fracture Mechanics 93 (2012) 239–262.

[43] J. J. C. Remmers, G. N. Wells, R. de Borst, A solid-like shell element allowing for arbitrary delaminations, International Journal for Numerical Methods in Engineering 58 (2003) 2013–2040.

[44] B. Mohammadi, D. Salimi-Majd, Investigation of delamination and damage due to free edge effects in composite laminates using cohesive interface elements, Engineering Solid Mechanics 2 (2014) 101–118.

[45] I. Guiamatsia, G. D. Nguyen, A generic approach to constitutive modelling of composite delamination under mixed-mode loading conditions, Composites Science and Technology 72 (2012) 269–277.

[46] J.-W. Simon, D. Höwer, B. Stier, S. Reese, J. Fish, A regularized orthotropic continuum damage model for layered composites: intralaminar damage progression and delamination, Computational Mechanics (2017) 1–17.

[47] C. Comi, S. Mariani, U. Perego, An extended fe strategy for transition from continuum damage to mode i cohesive crack propagation, International journal for numerical and analytical methods in geomechanics 31 (2007) 213–238.

[48] A. Orifici, , I. Herszberg, R. Thomson, Review of methodologies for composite material modelling incorporating failure, Composite Structures 86 (2008) 194–210.

[49] K. Park, G. H. Paulino, Cohesive zone models: A critical review of traction-separation relationships across fracture surfaces, Applied Mechanics Reviews 64 (2012) 1–20.

[50] R. Dimitri, M. Trullo, L. De Lorenzis, G. Zavarise, Coupled cohesive zone models for mixed mode fracture: A comparative study, Engineering Fracture Mechanics 148 (2015) 145–179.

[51] D. Höwer, B. A. Lerch, B. A. Bednarcyk, E. J. Pineda, S. Reese, J.-W. Simon, Cohesive zone modeling for mode I facesheet to core delamination of sandwich panels accounting for fiber bridging, Composite Structures j.compstruct.2017.07.005 (2017) (in press).

[52] D. Höwer, B. A. Lerch, B. A. Bednarcyk, E. J. Pineda, S. Reese, J.-W. Simon, Cohesive zone modeling for mode I facesheet to core delamination of sandwich panels accounting for fiber bridging, NASA/TM-2017-219470 (2017) 1–42.

[53] A. Turon, C. Dávila, P. Camanho, J. Costa, An engineering solution for mesh size effects in the simulation of delamination using cohesive zone models, Engineering Fracture Mechanics 74 (2007) 1668–1682.

[54] G. Dias, M. de Moura, J. Chousala, J. Xavierb, Cohesive laws of composite bonded joints under mode I loading, Composite Structures 106 (2013) 646–652.

[55] D. Xie, A. G. Salvi, C. Sun, A. M. Waas, A. Caliskan, Discrete cohesive zone model to simulate static fracture in 2D triaxially braided carbon fiber composites, Journal of Composite Materials 40 (2006) 2025–2046.

[56] C. G. Dávila, P. P. Camanho, C. A. Rose, Failure criteria for frp laminates, Journal of Composite Materials 39 (2005) 323–345.

[57] Hexcel Composites, A comprehensive guide to standard Hexcel honeycomb materials, configurations, and mechanical properties, Hexcel Corporation (1999).

[58] W. Broughton, Mechanical Testing of Advanced Fibre Composites, Woodhead Publisching Limited, 2000.

[59] C. Tsai, I. Daniel, Determination of in-plane and out-of-plane shear moduli of composite materials, Experiential Mechanics 30 (1990) 295–299.

[60] A. Nettles, Basic Mechanics of Laminated Composite Plates, NASA Refeference Publication 1351, 1994.

[61] J. G. Williams, On the calculation of energy release rates for cracked laminates, International Journal of Fracture 36 (1988) 101–119.

[62] F. A. Leone, D. Girolamo, C. G. Dávila, Progressive damage analysis of bonded composite joints, NASA/TM-2012-217790 (2012) 1–39.

[63] C. Harvey, M. Eplett, S. Wang, Experimental assessment of mixed-mode partition theories for generally laminated composite beams, Composite Structures 124 (2015) 10–18.

[64] C. Harvey, S. Wang, Experimental assessment of mixed-mode partition theories, Composite Structures 94 (2012) 2057–2067.

[65] S. Wang, C. Harvey, L. Guan, Partition of mixed modes in layered isotropic double cantilever beams with non-rigid cohesive interfaces, Engineering Fracture Mechanics 111 (2013) 1–25.

[66] C. Sarrado, A. Turon, J. Costa, J. Renart, An experimental analysis of the fracture behavior of composite bonded joints in terms of cohesive laws, Composites: Part A 90 (2016) 234–242.